thermo

MDPI

Technical Note

Artificial Intelligence Applied to Microwave Heating Systems: Prediction of Temperature Profile through Convolutional Neural Networks

Victor Rosario Núñez *, Alfonso Hernández, Iván Rodríguez, Ignacio Fernández-Pacheco Ruiz and Luis Acevedo

Idener Research and Development, 41300 Seville, Spain; alfonso.hernandez@idener.ai (A.H.); ivan.rodriguez@idener.ai (I.R.); luisenrique.acevedo@idener.ai (L.A.)
* Correspondence: victor.rosario@idener.ai

Abstract: Microwave heating, which is caused by the interaction of electromagnetic radiation and materials, has become an important component in industrial operations across numerous industries. Despite their importance, conventional numerical simulations of microwave heating are computationally intensive. Concurrently, advances in artificial intelligence (AI), particularly machine learning algorithms, have transformed data processing by increasing accuracy while decreasing computational time. This study tackles the difficulty of efficient and accurate modelling in microwave heating by combining convolutional neural networks (CNNs) with traditional simulation techniques. The major goal of this research is to use CNNs to forecast temperature profiles in a variety of industrial materials, including susceptors, semi-transparent, and microwave-transparent materials, under varying power settings and heating periods. This unique strategy greatly reduces prediction times, with up to 60-fold speed increases over standard methods. Our research is based on examining the electromagnetic and thermal responses of these materials under microwave heating. This study's findings emphasise the need for extensive datasets and show the transformational potential of CNNs in optimising material processing. It uses artificial intelligence to pave the way for more effective and exact simulations, supporting breakthroughs in industrial microwave heating applications.

Keywords: microwaves; modelling; CNN; materials; susceptors

check for updates

Citation: Rosario Núñez, V.; Hernández, A.; Rodríguez, I.; Fernández-Pacheco Ruiz, I.; Acevedo, L. Artificial Intelligence Applied to Microwave Heating Systems: Prediction of Temperature Profile through Convolutional Neural Networks. *Thermo* **2024**, *4*, 346–372. https://doi.org/10.3390/thermo4030018

Academic Editor: Johan Jacquemin

Received: 4 June 2024
Revised: 29 July 2024
Accepted: 30 July 2024
Published: 3 August 2024

Copyright: © 2024 by the authors. Licensee MDPI, Basel, Switzerland. This article is an open access article distributed under the terms and conditions of the Creative Commons Attribution (CC BY) license (https://creativecommons.org/licenses/by/4.0/).

1. Introduction

The application of microwave heating, originating from the intricate interplay between electromagnetic radiation and matter, has evolved from its modest beginnings in culinary applications to become a fundamental element of contemporary industrial operations across various industries [1,2]. Microwaves, defined as a type of electromagnetic radiation within the frequency range of 0.3 GHz to 300 GHz, correspond to a wavelength range of 0.001 m to 1 m. To avoid interference with medical and communication apparatus, most microwave processing equipment operates at frequencies of 2.45 GHz and 915 MHz [3].

Heat generation by microwaves depends on the reaction of materials to electromagnetic fields, predominantly through the interaction of polar molecules in dielectric materials [4]. These polar molecules oscillate in response to the electric field, causing intermolecular friction and producing thermal energy. This volumetric, in-situ heat generation accelerates processing compared to conventional methods, where heat is transferred from external sources [5]. Advanced microwave applications require considering various dielectric materials, including microwave-transparent, semi-transparent, and susceptor materials [2].

With the increasing integration of microwave heating into industrial processes, the demand for accurate and controllable temperature distributions within materials has surged. The complex interactions between electromagnetic fields, material properties,

and geometries pose significant challenges [6]. Numerical simulations, such as finite element analysis and computational electromagnetic modelling, have become essential for predicting temperature distributions [6]. These simulations allow for the optimisation of process parameters to achieve uniform heating and minimise undesired effects like hot spots and thermal gradients [7,8].

The examination of temperature forecasts during microwave heating represents a continuous endeavour to utilise electromagnetic waves for precise and effective heat regulation in various material processing fields [9]. Besides advanced simulations, machine learning can significantly increase the accuracy of result [8]. For instance, studies have employed machine learning techniques to analyse the frequency response of split-ring resonators and to classify processes like biomass microwave pyrolysis, enhancing the understanding and optimisation of these processes [10].

In another study, Lambert's law was used for power distribution calculations in microwave heating, but the complex environment posed limitations. Combining sliding mode control with neural network technology improved the safety and efficiency of the heating process [11]. Similarly, adaptive dynamic programming has been used to create intelligent temperature management methods, effectively regulating heating temperatures and ensuring consistent microwave power adjustment. Various machine learning methods, such as ANFIS, ANN, and RSM, have also been evaluated for predicting the optimum tensile strength of microwave post-cured composites [12].

Machine learning has improved the design of materials' geometry for microwave heating, showing significant efficiency improvements in product optimisation [13]. Additionally, the use of neural networks for modelling microwave applicators and predicting frequency and mode characteristics has demonstrated high accuracy and efficiency, highlighting the benefits of machine learning in this field [14]. Finally, studies have utilised machine learning to identify factors influencing the microwave dielectric properties of various ceramic structures, developing novel descriptors for characterising inorganic crystalline compounds [15].

In this context, the objective of the present work is to develop a straightforward yet sophisticated temperature estimator capable of calculating thermal profiles for various materials, including microwave-transparent, semi-transparent, and susceptors, operating at a frequency of 2.45 GHz. This study employs convolutional neural networks to analyse thermal and dielectric properties under various power levels and heating durations, aiming to enhance the efficiency and accuracy of microwave heating simulations.

2. Microwave Heating

The microwave model employed in this study to produce the datasets is derived from a prior publication by Acevedo et al., 2021 [2]. This paper introduces a unidimensional model that integrates the transient equations of electromagnetic phenomena with the heat transfer algorithms. The model has been solved using the finite-difference time-domain (FDTD) method [16].

In this sense, microwave heating can be described as the result of a molecular level interaction between a substance and an electric field. The outcome of this interaction gives rise to translational movements of charges that are either free or bound, as well as the rotation of dipoles. It offers a rapid, efficient, and precise way to heat materials, with heat distributed throughout the material's volume rather than relying on surface conduction [17].

The computation of microwave effects induced by an electromagnetic field on a material requires the employment of simulations. The first step involves the examination of electromagnetic fields as specified by Maxwell's equations and appropriate boundary conditions. The following equations present the differential form of the electromagnetic field's governing equations in the cartesian coordinate system (X, Y, Z).

$$\nabla \times \vec{E} = -\mu \frac{d\vec{H}}{dt} \dashrightarrow \begin{cases} \frac{\partial E_Z}{\partial y} - \frac{\partial E_Y}{\partial z} = -\mu \frac{\partial H_X}{\partial t} \\ \frac{\partial E_X}{\partial Z} - \frac{\partial E_Z}{\partial X} = -\mu \frac{\partial H_Y}{\partial t} \\ \frac{\partial E_Y}{\partial X} - \frac{\partial E_X}{\partial Y} = -\mu \frac{\partial H_Z}{\partial t} \end{cases} \tag{1}$$

$$\nabla \times \vec{H} = \epsilon \frac{d\vec{E}}{dt} \dashrightarrow \begin{cases} \frac{\partial H_Z}{\partial Y} - \frac{\partial H_Y}{\partial Z} = \epsilon \frac{\partial E_X}{\partial t} \\ \frac{\partial H_X}{\partial Z} - \frac{\partial H_Z}{\partial X} = \epsilon \frac{\partial E_Y}{\partial t} \\ \frac{\partial H_Y}{\partial X} - \frac{\partial H_X}{\partial Y} = \epsilon \frac{\partial E_Z}{\partial t} \end{cases} \tag{2}$$

Simplifying Maxwell's equations in one dimension involves the assumption that wave propagation occurs solely in one direction, simplifying the problem. Plane waves are unlimited in extent, therefore implying infinite power flow, and cannot occur in practice; however, these kinds of waves are considerably more controllable and highly useful to visualise practical field setups [18]. Despite the idealisation, one-dimensional plane waves offer a controllable and insightful model for practical field setups. They help visualise fundamental concepts like reflection, refraction, transmission, and absorption of waves and are crucial for designing and optimising communication systems and electromagnetic devices. Thus, the one-dimensional Maxwell equations are used due to their ability to effectively represent and analyse real-world applications, providing a balance between mathematical tractability and physical relevance [19].

The mathematical solution of the Maxwell equation for plane waves shows that one may assume, without loss of generality, that the electric field is in the Y-direction and the magnetic field is in the Z-direction when a planewave is travelling in the positive X-direction [x]. Consequently, there are no components of electric field in the Z- and X-directions ($E_X = 0$ $E_Z = 0$, $\frac{\partial}{\partial z} = 0$), and the components in the Y- and X-directions of the magnetic field are null ($H_Y = 0$ $H_X = 0$, $\frac{\partial}{\partial y} = 0$), which can be outlined in one-dimensional form as follows [6]:

$$\frac{\partial E_Z}{\partial X} = -\mu \frac{\partial H_Y}{\partial t} \tag{3}$$

$$\frac{\partial H_Y}{\partial X} = \varepsilon \frac{\partial E_Z}{\partial t} \tag{4}$$

In the preceding equations, the subindexes X, Y, and Z represent the vector components of E and H. The symbols μ and ε represent the magnetic permeability and electric permittivity, respectively.

In order to solve the Equations (3) and (4), as previously noted, the finite-difference time-domain (FDTD) method, adopted from [20], is applied to compute E and H. Constant coefficients are established and stored for each field vector component in an area where material qualities vary continuously with spatial position, prior to the time-stepping process as follows:

$$C_a = \frac{\left(1 - \frac{\sigma_i \Delta t}{2\varepsilon_0 \varepsilon_i}\right)}{\left(1 + \frac{\sigma_i \Delta t}{2\varepsilon_0 \varepsilon_i}\right)} \tag{5}$$

$$C_b = \left(\frac{\Delta t}{\mu_0 \Delta x}\right) \frac{\left(\frac{\Delta t}{\varepsilon_0 \varepsilon_i \Delta x}\right)}{\left(1 + \frac{\sigma_i \Delta t}{2\varepsilon_0 \varepsilon_i}\right)} \tag{6}$$

When there is a transition between two different materials, the pertinent dielectric characteristics, ε_i and σ_i, for Ez, located at the boundary plane between those materials, are described as follows:

$$\varepsilon_i = \frac{(\varepsilon_1 + \varepsilon_2)}{2} \tag{7}$$

$$\sigma_i = \frac{(\sigma_1 + \sigma_2)}{2} \tag{8}$$

Finally, the input source must be included to complete the electromagnetic effects computation.

$$E_{z(t)} = E_{z(t-1)} - \sqrt{\frac{4Z \cdot P_{in}}{A}} sin\left(\frac{\pi X}{W}\right) \cdot cos\left[2\pi\left(f \cdot t - \frac{X}{\lambda}\right)\right] \tag{9}$$

Here, E is the amplitude of the electric field produced by the microwave, which considers a commercial rectangular waveguide (i.e., WR340) and microwave power of 800 [W] as is shown in Equation (9), where f is the frequency, W is the width of the incident plane (waveguide), Z the wave impedance, λ the wavelength of the microwave in that waveguide, Pin the power input, and A is the waveguide area.

Equations (1)–(9) have been linked together to derive the electromagnetic algorithm with dynamic solutions based on FDTD [16,21]:

$$E_{z(i)} = C_{a(i)}E_{z(i)} + C_{b(i)}\left(H_{y(i)} - H_{y(i-1)}\right) \tag{10}$$

$$H_{y(i)} = H_{y(i)} + \left(E_{z(i)} - E_{z(i-1)}\right) \tag{11}$$

On the other hand, a set of heat transfer equations must be included to compute the temperature profile.

To calculate the internal heat generation due electric field presence (Equation (9)), the following equation can be used [4,9,17]:

$$\dot{Q}_{MW} = 2\pi f \varepsilon_o \varepsilon'(T)(tan\delta(T))E^2 \tag{12}$$

Q is the internal heat generation, f is the frequency, and ε is the dielectric constant (subindex 0 corresponds to free space). Here, $tan\delta(T)$ describes the behaviour of electromagnetic waves inside the material in terms of penetration (dielectric constant $\varepsilon'(T)$) and absorption (dissipation factor ε''(T)) in a temperature-dependent way as follows [9]:

$$tan\delta(T) = \frac{\varepsilon''(T)}{\varepsilon'(T)} \tag{13}$$

Once heat generation is calculated, the heat conduction equation determines temperature distribution. This equation can be represented in its general form as follows:

$$\frac{\partial T}{\partial t} = \alpha \Delta^2 T + \frac{\dot{Q}_{MW}}{\rho Cp} \tag{14}$$

Here, ρ is the density, Cp is the specific heat, and α is the thermal diffusivity. In addition, κ is the thermal conductivity, which is defined as follows:

$$\alpha = \frac{\kappa}{\rho Cp} \tag{15}$$

Finally, the FDTD for heat equation to compute the variation of temperature T in time t can be represented considering transient one-dimensional heat conduction in a plane of the piece material with thickness L and heat generation Q_{MW} (changing with time and position) as follows:

$$T_{i-1} - 2T_i + T_{i+1} + \frac{\dot{Q}_{MW}\Delta z^2}{\kappa} = \frac{\Delta z^2}{\alpha \Delta t}\left(T_i^{n+1} - T_i^n\right) \tag{16}$$

The simulation calculates the solutions to Equations (10), (11) and (16) in order to obtain the entire dataset of the electromagnetic field solution and its thermal effects on materials. In order to achieve detailed results, it is necessary to minimise the size of both space Δz and time Δt steps. However, this might significantly increase the computational

time, hence slowing down the process of testing and comparing different materials. Nevertheless, as mentioned in Section 1, the temperature obtained can be represented faster using machine learning methods. The work has built a machine learning system that can accurately simulate the thermal effects described in reference [2] by reducing electromagnetic and thermal Equations (1)–(16). This signifies a decrease in computational resources, leading to a 60-fold enhancement in the speed of acquiring outcomes. The techniques employed are elucidated in the following subcategory.

3. Machine Learning Approach

Herein, a novel framework comprising multiple neural network modules is introduced, each meticulously tailored to represent microwave heating materials within this study.

To accurately navigate the temporal intricacies of microwave-induced heating patterns described in previous equations, the methodology presented harnesses the strengths of convolutional neural networks (CNNs). These networks are renowned for their proficiency in pattern recognition within visual domains, yet their application extends far beyond, proving equally potent in identifying and learning from temporal sequences. By treating time as a spatial dimension, CNNs are uniquely equipped to unravel the sequential dependencies and features within the simulated microwave heating data, like they would discern patterns within an image as described in [22].

As explained by [23,24], a neuron's receptive field is the region of the input space that a particular feature map covers after the convolution operation. The network extracts local spatial features by convolving learnable filters with these receptive fields. These features capture patterns such as edges and shapes in different parts of the input matrix.

Finally, the maps, or feature maps, represent the features the network have detected at each layer. Each feature map is a new representation of the input data, focusing on specific attributes highlighted by the filter applied in that layer, as represented in Figure 1.

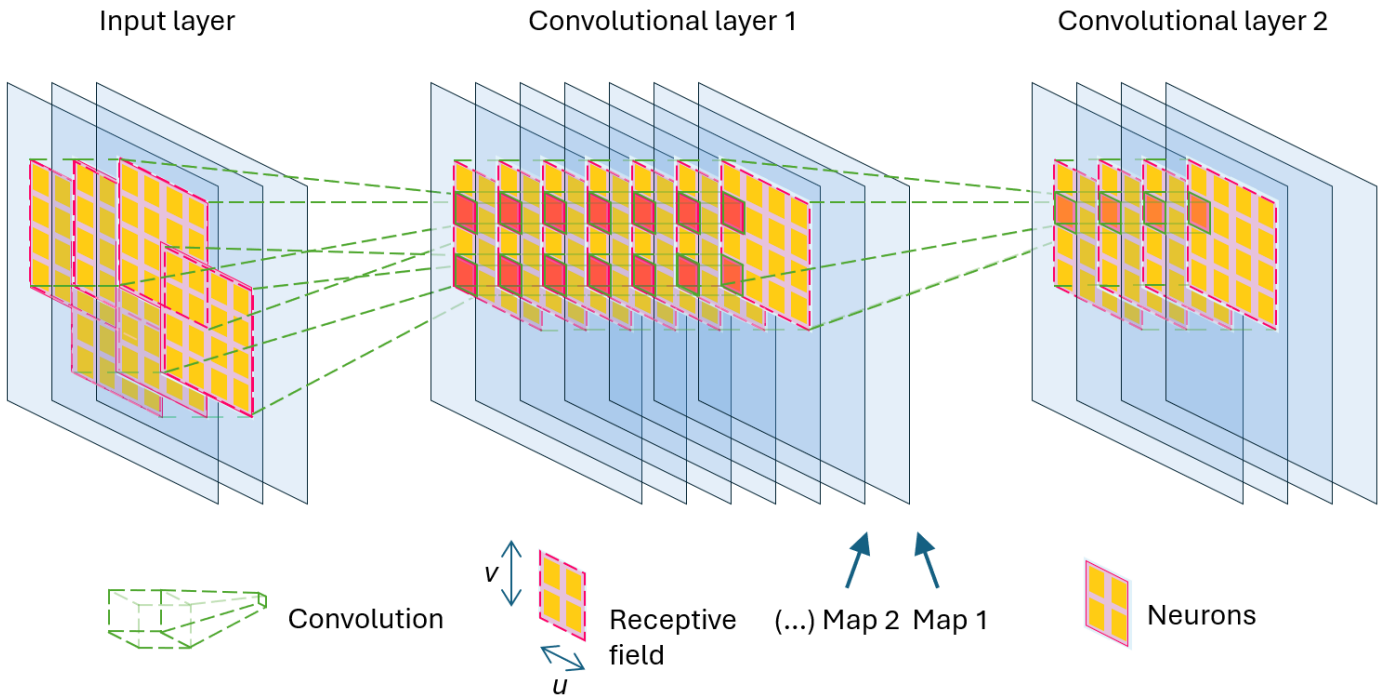

Figure 1. Convolutional layer representation.

Pooling layers are a component of convolutional neural networks used to reduce the spatial dimensions of the feature maps generated by convolutional layers. By performing down-sampling, pooling layers help reduce the number of parameters and computational complexity while also making the features extracted by the convolutional layers more robust to variations in the position of features in the input. The pool size specifies the dimensions of the region over which the pooling operation, such as taking the maximum (MaxPooling) or average (average pooling), is applied.

Incorporating a MaxPooling layer after each convolutional layer serves a dual purpose. First, they significantly reduce the spatial dimensions of the feature maps, thereby diminishing the computational load and the risk of overfitting by abstracting the most essential features. This reduction is achieved by selecting the maximum value from each patch of the feature map covered by the pooling window (Figure 2). Second, MaxPooling enhances the network's invariance to minor shifts and distortions in the temporal patterns. This characteristic is crucial for generalising effectively across various material responses to microwave heating, as it allows the model to recognise pertinent patterns despite variations in the heating time or power used.

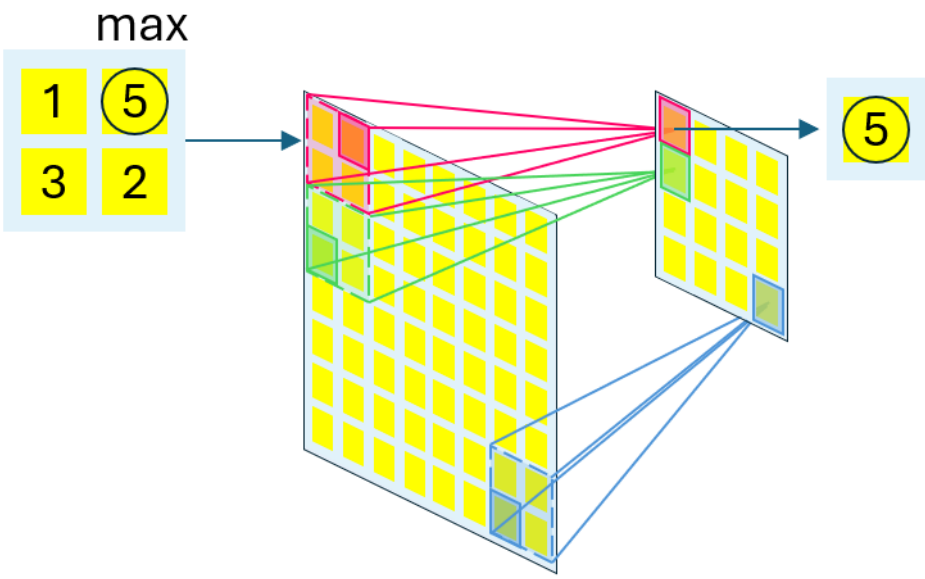

Figure 2. Convolutional layer connected to the MaxPooling layer.

At this point, the input data have been synthesised into high-dimensional outputs; nevertheless, the required output from this model is a one-dimensional array in which different temperatures are predicted. A flattening layer achieves the expected output (Figure 3). Flatten layers are utilised to transform the multi-dimensional output of convolutional layers into a one-dimensional vector. This transformation is crucial as it allows the spatially structured feature data to be input into dense layers, which are fully connected and responsible for further processing and pattern recognition. This step is essential for marrying the spatial feature extraction capabilities of CNNs with the pattern recognition prowess of dense layers [25].

Dense layers, also known as fully connected layers, play a crucial role in neural networks by integrating the features extracted by previous layers, such as convolutional and flattening layers. These layers consist of neurons connected to every activation during the last layer, enabling them to learn complex patterns from the data by considering the full context of the inputs. These fully connected layers will end up in the previously mentioned output, enabling seamless spatial and temporal data analysis integration within a singular framework.

Having previously stated the principal components of the neural networks, it is time to describe the final structure and justify the hyperparameter choices.

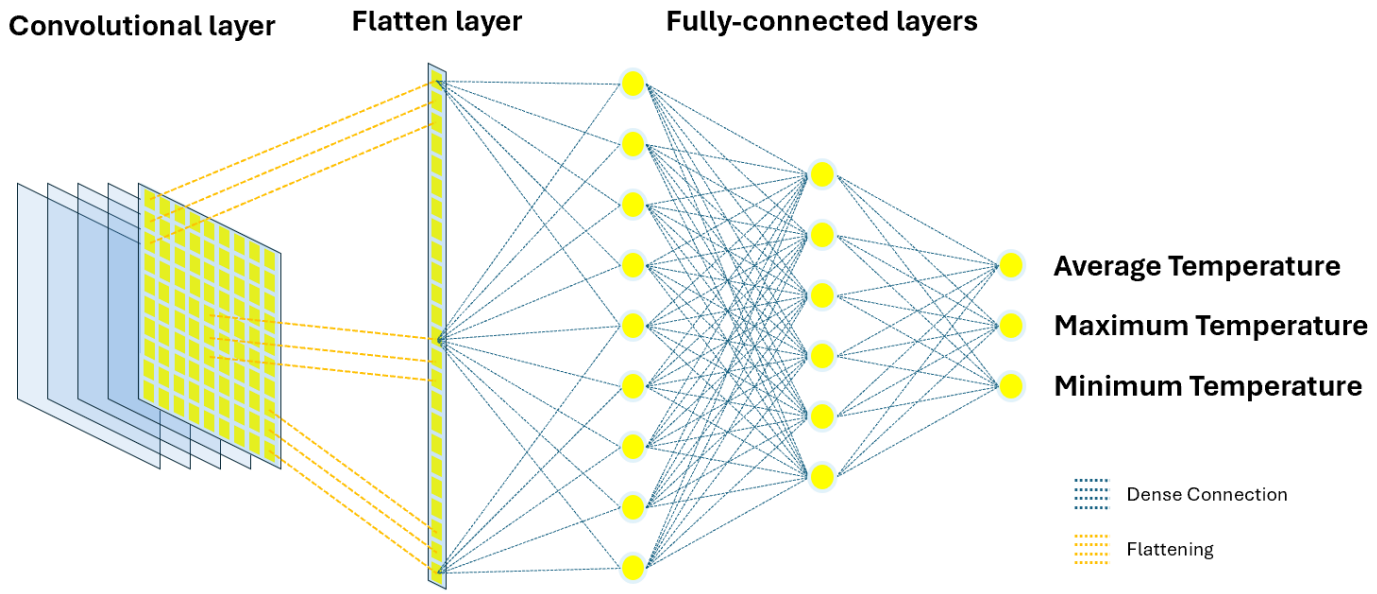

Figure 3. CNN top structure: Transition from CNNs to dense layers.

In this study, which focuses on materials heated from a baseline temperature of 25 degrees, the choice of ReLU (rectified linear unit) neurons offers better performance. The ReLU activation function is defined as Equation (17), which aligns with the temperature measurements starting from 25 degrees upwards.

$$f(x) = \max(0, x) \tag{17}$$

The best responses were given by the models with two convolutional layers, each followed by one MaxPooling layer, and ended with three fully connected dense layers. For the convolutional layers, the number of maps is 128 and 64, respectively, and for the dense layers, the number of neurons is 50, 16, and 3. The final layer size is mandatory to meet the expected output.

To avoid overfitting, as the MaxPooling layers do with the convolutional layers, the regulariser L2 (also known as ridge regression [26]) was included in the dense layers. It prevents coefficients of linear regression models with many correlated variables from being poorly determined and exhibiting high variance. This type of regularisation allows models to enhance the capacity of generalisation.

The last mention of the model hyperparameters is related to kernel and pool size. For both, one length of the kernel is fixed to a size of two due to the shape of the given input, composed of two arrays, one representing the time step and the other the power used. The other dimension was treated as a hyperparameter as it could be optimised. As a result, the best performance was obtained for a size of two, which means that square kernel and pool filters were applied.

In Figure 4, the final model architecture shows the overall network architecture and data flow through the different layers composing the neural network. As explained above, each component in the network fulfils a specific purpose, and its design is optimised to achieve optimal results in forecasting material temperatures using power time series data.

The network architecture facilitates extracting and refining information as data flows through it. The figure shows two main blocks: the bottom block, which extends until the flattening layer, and the top block, which extends from the flattening layer to the output layer.

The network's bottom block comprises two stacked blocks, each composed of one CNN followed by a MaxPooling layer. Each of these blocks applies the CNN kernels to increase the level of data abstraction. At the same time, the MaxPooling layer reduces

the spatial dimensions of the resulting tensors, thus simplifying the information while retaining the most significant features.

This combination adheres to efficiency criteria in improving the model's generalisation capabilities, thus reducing the computational load and simplifying the model.

The top block of the neural network starts with the flattening layer, which will receive the resulting tensor output from the bottom block in (4, 64) and yield a one-dimensional array of 256. Then, the information is ready to flow through the dense layers, which, equipped with an L2 regulariser to prevent overfitting, will finally yield the three temperature values: average, maximum, and minimum.

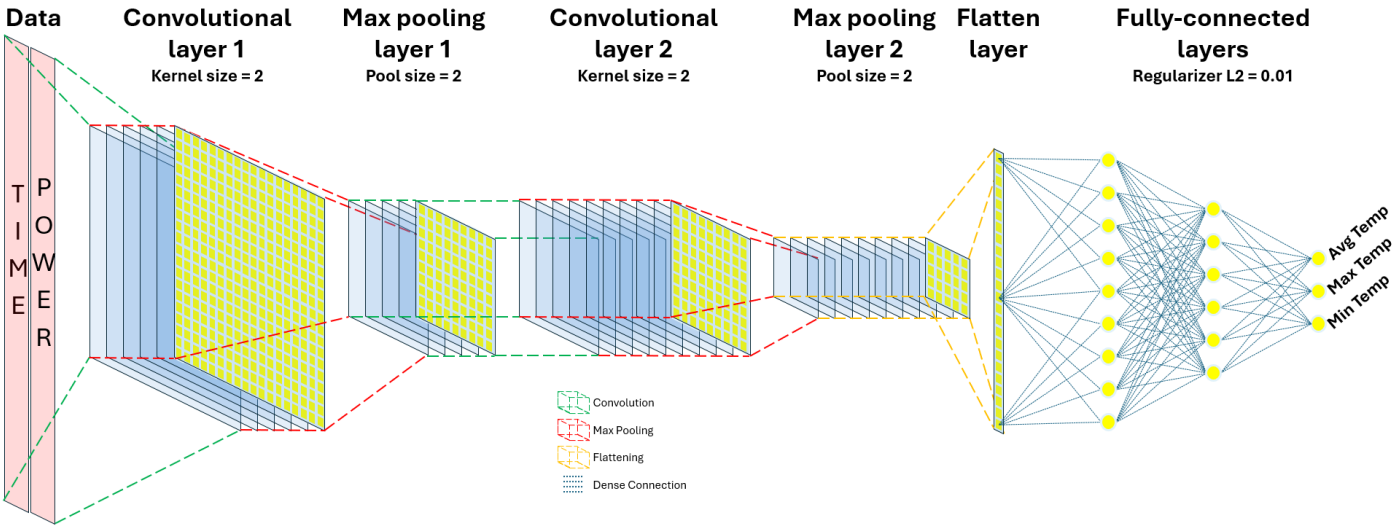

Figure 4. Final model architecture.

Once the models have been developed, it is imperative to ensure that they generalise well to unseen data. Cross-validation [27] is a statistical method that is crucial in achieving this objective. Cross-validation comprehensively evaluates the model's performance by partitioning the dataset into multiple subsets and iteratively training and validating the model on these subsets. This technique mitigates the risk of overfitting, which occurs when a model learns the noise in the training data rather than the underlying patterns. Moreover, cross-validation offers an unbiased estimate of model performance by leveraging different data splits, thus providing a more accurate assessment than a single train-test split. Consequently, the use of cross-validation enhances the reliability and robustness of machine learning models, ensuring they perform well on both training and unseen data. Therefore, implementing cross-validation is essential for developing models that are both accurate and generalisable.

4. Dataset Description

The machine learning segment of our research harnesses advanced algorithms to interpret the rich and nuanced data derived from extensive simulations. The data were sourced from the simulator proposed by [2]; it extracted the simulation time, the microwave power applied and the temperatures (average, maximum, and minimum). No other data were introduced during the development nor the validation, as the principal purpose of this study is to enhance the performance of an already developed simulator in what time refers to, being the temperature prediction carried out by the mathematical simulations the slower process.

The simulator has been adapted to provide the data needed to apply the CNN algorithm. In this sense, the time step applied for computing the heating patterns was modified

to increase the number of results, thereby increasing the prediction accuracy of the CNNs using the following formula:

$$Tdt = \frac{dx^2}{(2 \times alpha)} \times 0.1 \tag{18}$$

where:

$$dx = \frac{c}{\frac{v}{x}} \tag{19}$$

The variables are defined as follows:

- c: Light speed
- v: Wave frequency
- x: The number of samples
- *alpha*: The thermal diffusivity of the material

As can be noticed from Equation (18), time steps may vary along with the material being simulated, producing variations in the number of records taken for each material and, therefore, resulting in datasets of different sizes. The dataset size is obtained using the equation below:

$$Dataset\ Size = N \times \frac{1}{\left(\frac{dx^2}{2 \times alpha \times 0.1}\right)} \tag{20}$$

where N corresponds to the simulated time in seconds for the chosen material.

Since not all the materials behave the same, and to get datasets of the same size and characteristics, it was decided to make the time steps variable with the motivation of balancing the datasets. To attain this goal, Equation (18) was parametrised as shown below:

$$Dataset\ Size = N \times \frac{1}{\left(\frac{dx^2}{2 \times alpha \times Z}\right)} \tag{21}$$

By setting the variable Z, it enables us to achieve equality in the size of datasets. The Z value was computed for all materials, defining the size of the dataset equal to 250,000 registries, and the equation is provided as follows:

$$Z = \frac{250,000 \times dx^2}{2 \times alpha \times N} \tag{22}$$

Finally, the dataset obtained includes the power, the simulated time, and temperatures (average, maximum, and minimum) for each material under study. Table 1 provides a dataset example extracted from ALN material. The rest of the materials will be obtained from the three material groups previously mentioned: (i) susceptors: ALN compact powder, CuO compact powder, and SiC; (ii) semi-transparent materials: soda lime glass, alumina silicate, borosilicate glass, and alumina cement; and (iii) transparent materials: boron nitride and dense mullite. For details on the materials, please see reference [2].

Table 1. Dataset example from ALN material.

N° Sample	Power (W)	Time (s)	Avg Temp. (°C)	Max Temp (°C)	Min Temp (°C)
1	100	0.028	25.016	25.048	25
2	100	0.055	25.032	25.087	25.000
3	100	0.083	25.048	25.120	25.000
4	100	0.111	25.064	25.154	25.000
...	...	...	...	...	...
215,588	2000	3.99869	347.9283	552.9065	204.86
215,589	2000	3.999344	348.0554	553.0815	204.9478
215,590	2000	3.999999	348.1824	553.2565	205.0356

5. Results

This section describes the implementation of the algorithm introduced in Section 3. The model explores the thermal behaviour (average, maximum, and minimum temperatures) of nine materials under identical conditions [2] (MW source from 100 W to 500 W, geometry, and initial temperature of 25 °C), as shown in Figure 5. The CNN's model reaches its objective when one of two conditions is met: an average temperature of 800 °C or 120 s of heating.

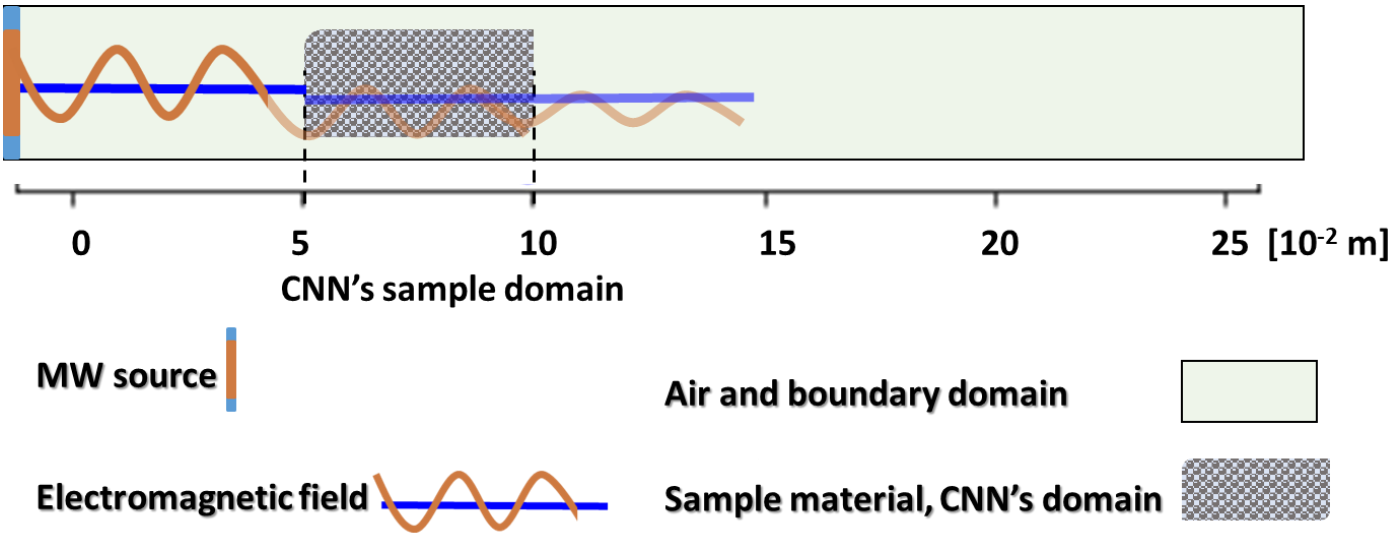

Figure 5. Graphical description of the microwave system modelled using CNNs.

The metrics followed to evaluate the models performance and robustness were precision, the mean absolute error, and the maximum absolute error. Nevertheless, the metric chosen was composed to train the model, taking the mean from the maximum absolute error and the mean squared error from the models and applying it to the previously introduced cross-validation to maintain predictions generally close to the material curve while avoiding overfitting.

5.1. Transparent Materials

5.1.1. Boron Nitride

In Figure 6, boron nitride comparison curves show the three temperatures, average, maximum, and minimum obtained in the CNN domain shown in Figure 5 and compare these values with actual data from the complete electromagnetic and thermal simulation [2].

The model demonstrates good alignment with the actual data, indicating a more accurate performance during periods of steeper temperature increase. This is observed mainly when simulating high microwave power. For low power rates, small differences of no more than 0.2 °C are noted between the model's predictions and the actual temperature readings at the end of the simulation.

Average Temperature Curves

Both the actual and predicted temperatures show a consistent and gradual increase over time. The model closely follows the actual temperature trend, suggesting it has captured the material's thermal response to this power setting well. For higher power rates (>300), the prediction closely mirrors the actual temperature's upward trajectory, with a slightly steeper slope. This may indicate that the model is slightly overestimating the heat capacity or underestimating the heat dissipation rate for the material. However, the convergence of the prediction with the actual values over time suggests that the model adjusts well as it receives more data points.

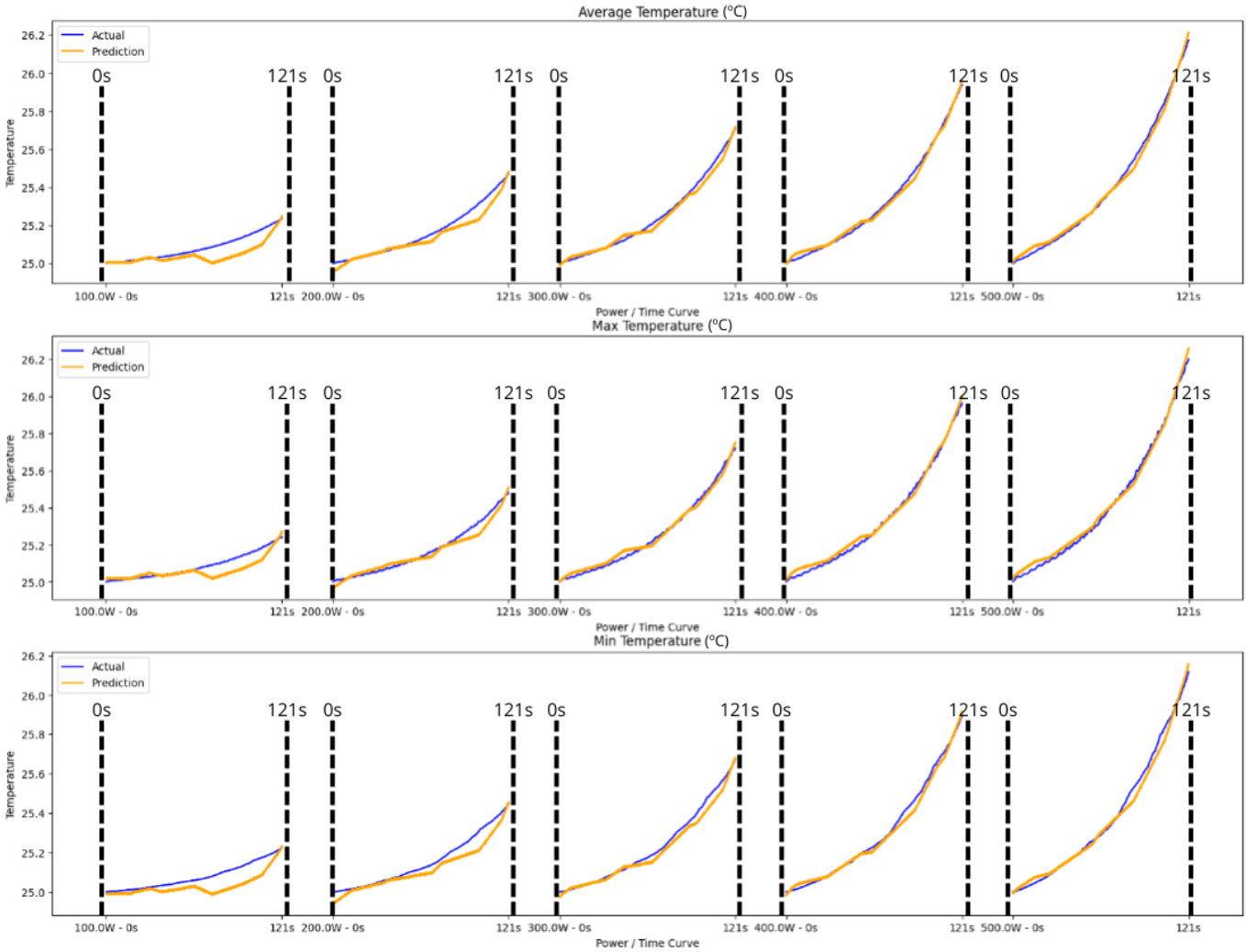

Figure 6. Boron nitride comparison curves.

Maximum Temperature Curves

The predictions closely follow the actual temperatures, with a minor overestimation of 0.2 °C in the mid-section of the curves. This might indicate that the model expects the material to retain heat more than it does. Yet, the model accurately captures the thermal behaviour trend, which is a positive indication of its learning from the material's response.

Mininimum Temperature Curves

The prediction and actual curves align closely, with the prediction slightly lower in the latter half. This implies that the model might be slightly conservative in estimating temperature increases, possibly due to a high emphasis on the material's initial thermal characteristics. There is a consistent pattern where the model slightly underestimates the temperature before aligning more closely as time progresses. The initial lag could be due to a delayed thermal response within the model's parameters.

From this simulation, the following metrics are obtained and shown in Table 2:

Table 2. Boron nitride model metrics.

	Mean Temperature (°C)	**Max Temperature (°C)**	**Min Temperature (°C)**
Mean Absolute Error	0.022	0.024	0.027
Max Absolute Error	0.327	0.326	0.290
Mean Squared Error	0.001	0.001	0.001

The MAE values across the mean, maximum, and minimum temperature predictions are remarkably low, with values of 0.022 °C, 0.024 °C, and 0.027 °C, respectively. This indicates a high level of precision in the model's predictions, with an average deviation from actual temperatures being mere hundredths of a degree. Such precision is commendable and indicates that the model is well-tuned to predict temperature fluctuations with minimal error.

The maximum errors recorded are 0.327 °C, 0.326 °C, and 0.290 °C. While these values are higher than the MAE, it is important to note that they represent the worst case deviations in the model predictions. Considering the potential variability and complexities involved in predicting temperature changes in different materials, these maximum absolute error values suggest that even in the most challenging scenarios, the model maintains a reasonable level of accuracy.

The MSE values for all three temperature predictions stand uniformly at 0.001 °C. This metric, emphasising the square of the errors before averaging, indicates that the model consistently maintains a tight bound on errors, with very few large deviations. A low MSE is particularly impressive as it suggests not only that the average error is low but also that the distribution of errors skews towards smaller, less impactful mistakes.

5.1.2. Dense Mullite

Dense mullite is also a transparent material, as can be observed in Figure 7. Dense mullite comparison curves were generated. In all the temperature curves, the model's predictions are quite close to the actual temperatures, reflecting the CNN's robust understanding of the material's thermal response. Such predictive accuracy is indicative of a well-developed model that captures the nuances of temperature change in response to varied power inputs.

Average Temperature Curves

Both actual and predicted curves begin closely aligned, indicating the model's accurate response to the initial thermal behaviour. As time progresses, the prediction slightly overestimates the temperature (>1.5 °C) in low power rates. This could mean that the model may be slightly conservative in its heat accumulation estimation for the material at this power level. Across higher power rates, the predictions are very close to the actual temperatures, particularly in the mid-section of the time series. The prediction slightly leads the actual temperature, potentially indicating the model's expectation of a quicker thermal response from the material than observed. The close tracking throughout suggests that the model has a good grasp of the thermal dynamics at play.

Maximum Temperature Curves

The prediction closely follows the actual curve with impressive accuracy. A slight overestimation is noted as the curve progresses (<1.5 °C), hinting that the model might slightly overpredict heat retention in the material at this low power setting. For high-power simulations, the model closely matches the actual temperature trend, with minimal overestimation at higher temperatures. This suggests that the model is well-calibrated to the material's response to increased power levels, though it may slightly overestimate the thermal conductivity or heat capacity of the material.

Minimum Temperature Curves

The prediction consistently tracks the actual temperature with high fidelity, indicating the model's robustness in understanding the material's response to varying energy inputs. The model seems particularly adept at capturing the rate at which the material cools down or its initial thermal inertia.

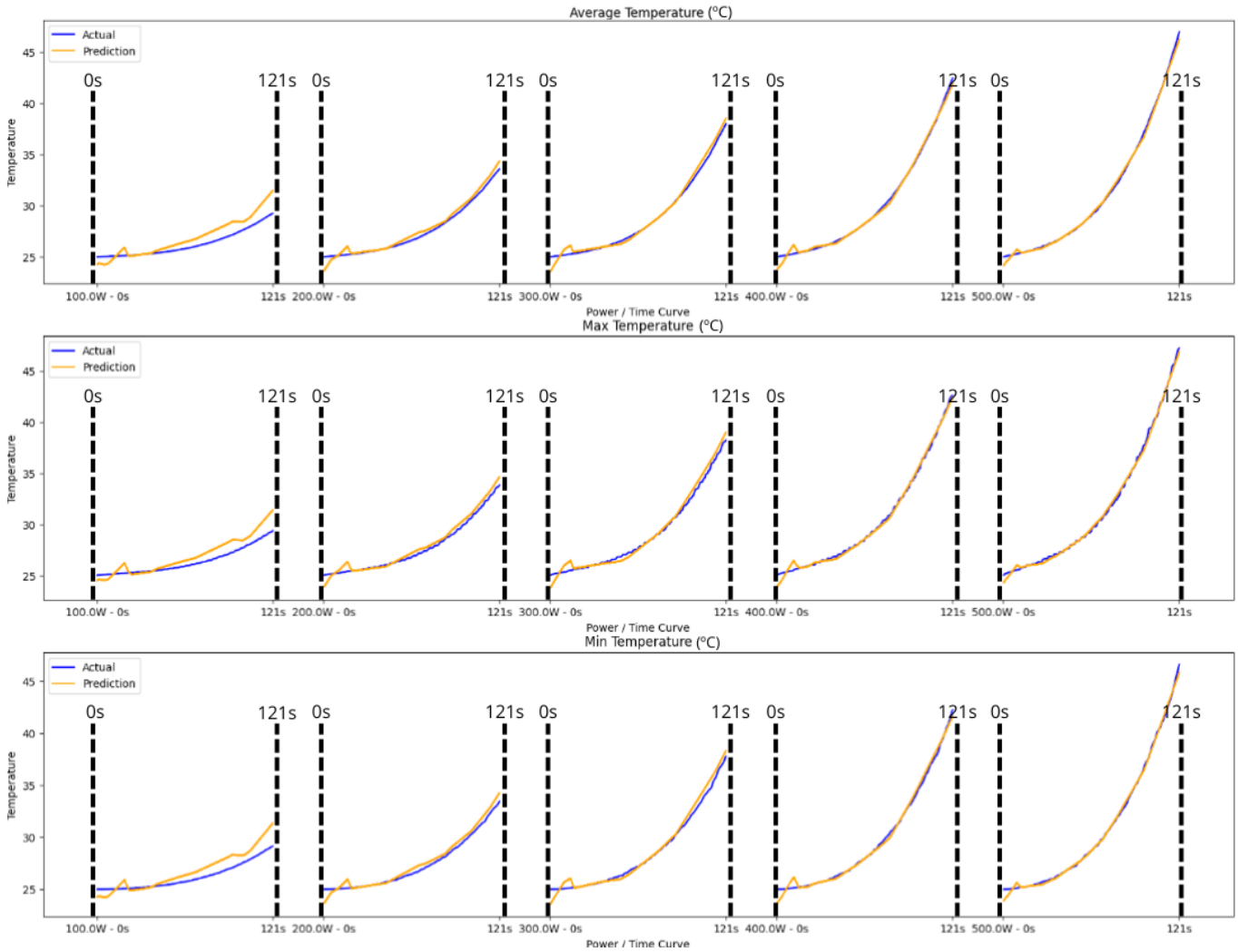

Figure 7. Dense mullite comparison curves.

The dense mullite model metrics extracted from the study of this material are expressed in Table 3.

Table 3. Dense Mullite Model Metrics.

	Mean Temperature (°C)	Max Temperature (°C)	Min Temperature (°C)
Mean Absolute Error	0.631	0.678	0.623
Max Absolute Error	13.837	14.933	13.348
Mean Squared Error	1.268	1.477	1.225

With MAE values of 0.631 °C for mean temperature, 0.678 °C for maximum temperature, and 0.623 °C for minimum temperature, the model demonstrates a commendable level of average accuracy across all temperature ranges. These figures suggest that, on average, the model's temperature predictions deviate from actual measurements by a small margin. Such performance is indicative of a well-constructed model that can reliably capture the general thermal behaviour of the new material.

The maximum absolute error values, recorded at 13.837 °C for mean temperature, 14.933 °C for maximum temperature, and 13.348 °C for minimum temperature, are not uncommon in predictive modelling, especially when dealing with materials that exhibit complex thermal responses.

The MSE values of 1.268 °C for mean temperature, 1.477 °C for maximum temperature, and 1.225 °C for minimum temperature further reinforce the model's consistent performance.

The model demonstrates good predictive performance with all temperatures. The errors are quite low, indicating that the model captures the overall trends and the nuances in the temperature data well. The similar MAE and MSE values across different temperature readings suggest a balanced model that does not disproportionately struggle with any aspect of temperature prediction.

5.2. Semi-Transparent Materials

5.2.1. Soda Lime Glass

In Figure 8, soda lime glass curves show how the heating curves of temperature values for soda lime glass differ. The material's response to heat appears complex and includes sudden changes caused by the non-linearities present in the data that challenge the modelling process.

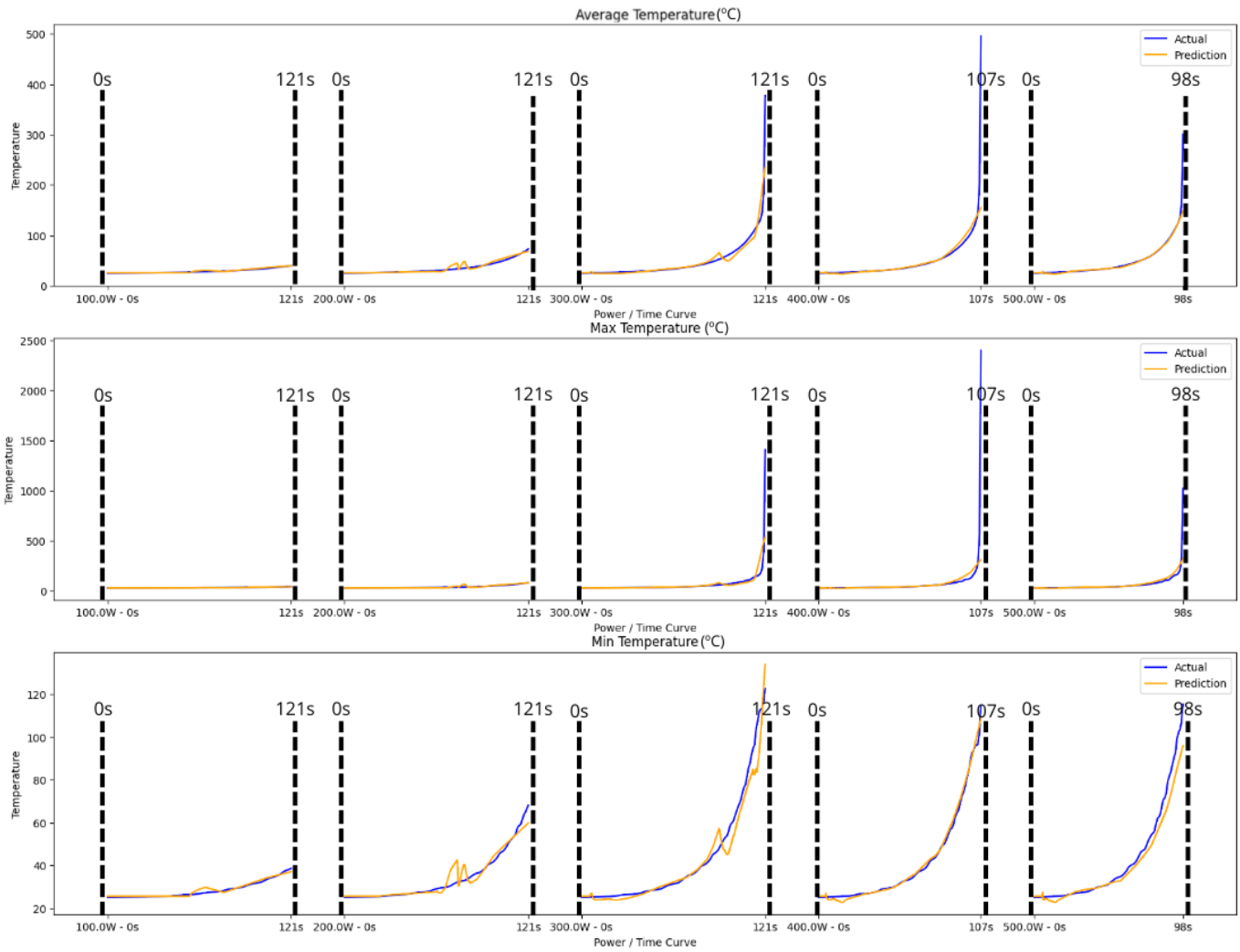

Figure 8. Soda lime glass curves.

Average Temperature Curves

The prediction closely mirrors the actual temperature, except for a minor lag at the end. This could mean that the model slightly underestimates the rate at which the material reaches its maximum temperature under high-power conditions. As the power increases, the model maintains a strong correlation with the actual temperature, reflecting its ability to scale its predictions appropriately with the increase in power. There is a slight lag in the prediction at the start, suggesting initial conditions or response time could be further calibrated.

Maximum Temperature Curves

The model's predictions are well-aligned with the actual temperature, showing only minor deviations. The model seems well-tuned to the material's thermal properties under these conditions. However, there is a notable discrepancy at the final temperature, where the model underestimates the actual temperature. This suggests that at very high power levels, the model may not fully account for the material's heat retention or the rate of temperature increase.

Minimum Temperature Curves

The prediction captures the actual trend with high fidelity, indicating that the model's understanding of the material's thermal response is quite robust at lower to mid-range power settings. At higher powers, the prediction slightly overshoots the actual temperature during the cooling phase, suggesting that the model might overestimate the material's ability to retain heat as the power setting increases.

As can be observed in soda lime glass model metrics presented in Table 4, the higher the temperatures are, the less accurate the model is.

Table 4. Soda lime glass model metrics.

	Mean Temperature (°C)	**Max Temperature (°C)**	**Min Temperature (°C)**
Mean Absolute Error	4.871	23.615	2.16
Max Absolute Error	693.082	4034.911	33.239
Mean Squared Error	666.814	22,163.493	13.868

The MAE values of 4.871 °C for mean temperature, 23.615 °C for maximum temperature, and 2.16 °C for minimum temperature reflect the model's capability to approximate temperatures with a degree of precision that, while varied across different temperature ranges, offers a foundational level of accuracy.

The maximum AE demonstrates a significant range, from 33.239 °C in minimum temperature predictions up to 4034.911 °C in maximum temperature predictions. While these errors initially may seem high, they also indicate the model's potential to identify and learn from extreme outliers.

The MSE values, particularly the high value observed in maximum temperature predictions, underscore the model's sensitivity to large deviations.

The model shows promising performance in predicting minimum temperatures, as reflected by the relatively lower error metrics, showcasing its strengths in handling at least some aspects of the temperature range.

5.2.2. Alumina Cement

The alumina cement curves are represented in Figure 9. The alumina cement comparison curves show that the temperature differences for this material are less abrupt than that noted for soda lime glass, and the model has much more precision representing the heating curves even when the difference between the maximum and the minimum is 200 °C.

Average Temperature Curves

The predictions show remarkable congruence with the actual temperatures, indicating that the model has effectively captured the relationship between the power applied and the resultant temperature increase.

Maximum Temperature Curves

The model demonstrates an excellent fit with the actual temperature. It captures the trend accurately, although it consistently predicts a marginally lower temperature (<2 °C). This might suggest that the model slightly underestimates the peak temperature response of the material or could be accounting for the faster dissipation of heat at higher temperatures.

Minimum Temperature Curves

The prediction closely aligns with the actual temperatures, reflecting the model's robust predictive capability for the material's behaviour at varying power levels.

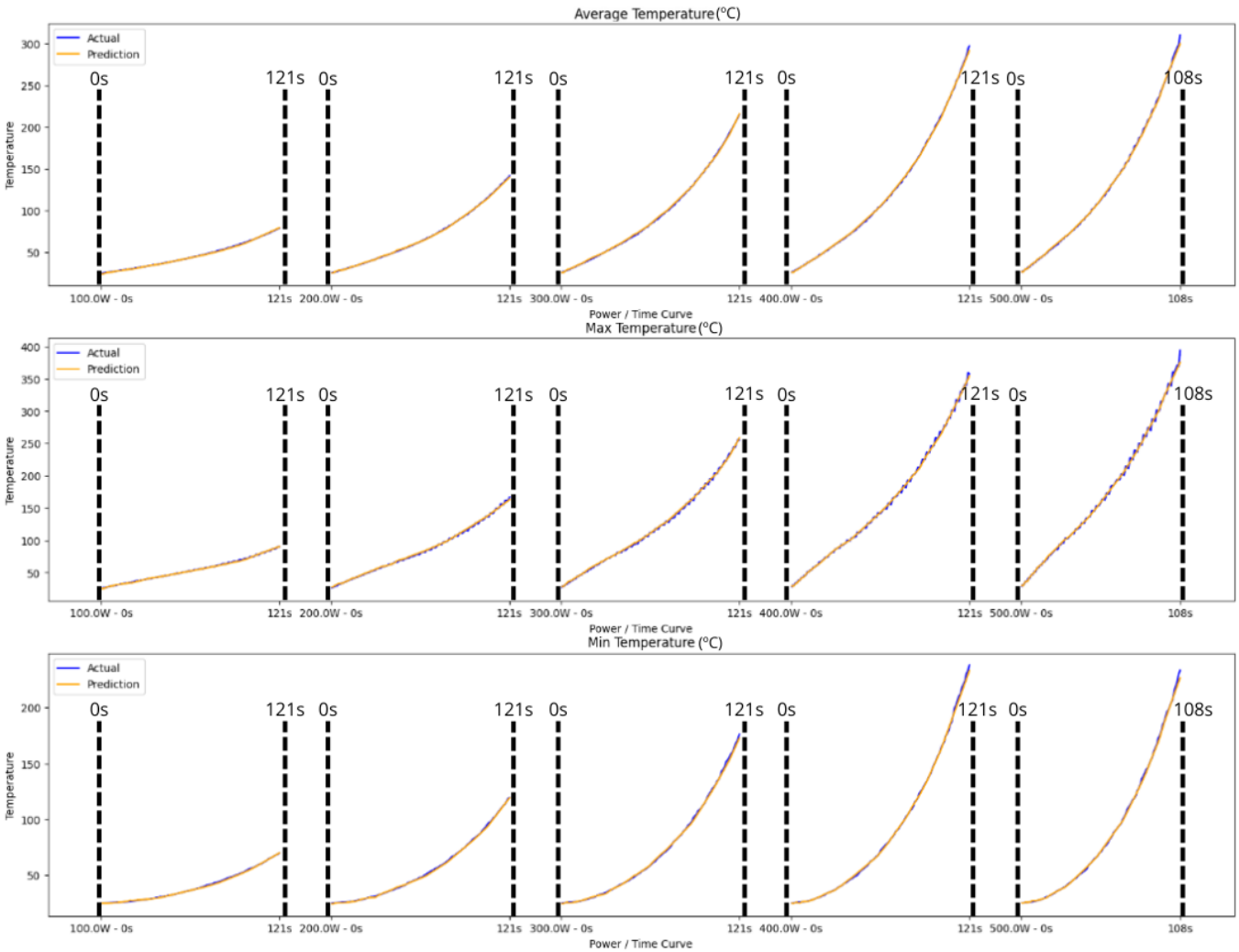

Figure 9. Alumina cement comparison curves.

Table 5 presents the alumina cement model metrics obtained for alumina cement.

Table 5. Alumina cement model metrics.

	Mean Temperature (°C)	**Max Temperature (°C)**	**Min Temperature (°C)**
Mean Absolute Error	1.129	2.475	0.802
Max Absolute Error	16.548	37.921	7.165
Mean Squared Error	2.851	15.098	1.357

The MAE values of 1.129 °C for mean temperature, 2.475 °C for maximum temperature, and 0.802 °C for minimum temperature showcase the model's commendable accuracy in its predictions. Particularly noteworthy is the model's precision in predicting minimum temperature, where the error is less than one degree. This level of precision indicates the model's effectiveness in capturing and predicting the lower range of temperatures with high reliability.

For instance, at the maximum AE values, the maximum error in minimum temperature predictions is significantly lower than that for maximum temperatures, suggesting that the model maintains a tighter control over predictions at the lower end of the temperature spectrum.

The MSE values across the board, with 2.851 °C for mean temperature, 15.098 °C for maximum temperature, and 1.357 °C for minimum temperature, point to the model's overall consistency in performance, with a particularly strong showing in the minimum temperature domain.

The model shows a reasonable level of accuracy with the lowest errors in predicting minimum temperatures and the highest errors for maximum temperatures. The moderate maximum absolute error for mean temperature and the high maximum absolute error for the maximum temperature indicate that while the model is generally reliable, it does occasionally make significant errors, especially with peak temperatures. The MSE values support this, showing more considerable variability in the errors for maximum temperatures.

5.2.3. Borosilicate Glass

Figure 10 shows borosilicate glass comparison curves. The borosilicate glass results show that, while not significantly changing, the small noise brought about by the maximum temperature curves somewhat upends the model's prediction.

Average Temperature Curves

There is an excellent alignment between predicted and actual temperatures, indicating that the model scales its predictions effectively with increased power. The predictions accurately mirror the actual temperatures, showing an understanding of the material's thermal characteristics across a range of operating conditions.

Maximum Temperature Curves

The model closely matches the actual temperature profile at these power levels, accurately capturing the material's response to higher energy inputs. It tracks the rising slope and peak temperatures effectively, with minimal discrepancies.

Minimum Temperature Curves

Predictions remain closely aligned with the actual data, with a very slight underestimation in the early phase of the heating cycle. This tight correlation showcases the model's robust performance across various power inputs.

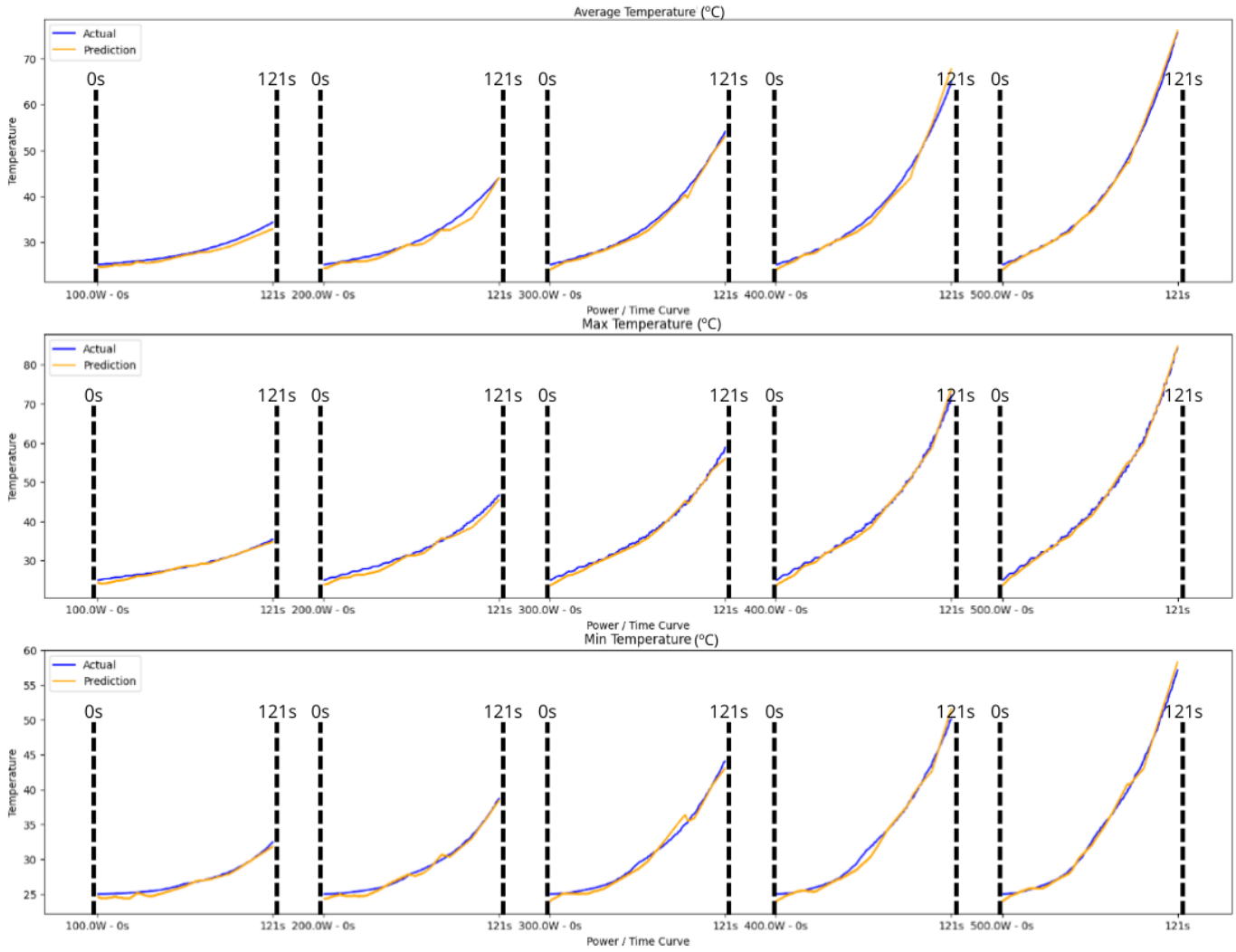

Figure 10. Borosilicate glass comparison curves.

The borosilicate glass model metrics are provided in Table 6. The metrics indicate that the general conduct of the curves has been assimilated, but there are some irregularities missing.

Table 6. Borosilicate glass model metrics.

	Mean Temperature (°C)	Max Temperature (°C)	Min Temperature (°C)
Mean Absolute Error	0.826	1.073	0.747
Max Absolute Error	21.952	34.833	10.680
Mean Squared Error	2.044	4.442	1.753

With MAE values of 0.826 °C for mean temperature, 1.073 °C for maximum temperature, and 0.747 °C for minimum temperature, the model exhibits a commendable level of accuracy across all temperature predictions. These figures are particularly impressive, indicating that, on average, the model's predictions are very close to the actual temperature measurements.

The maximum absolute error values provide insightful indicators of the model's performance under extreme conditions. The fact that these errors are contained within reasonable limits (21.952 °C for mean temperature, 34.833 °C for maximum temperature, and 10.680 °C for minimum temperature) underscores the model's robustness.

The MSE values reinforce the model's consistency in performance across different temperature predictions. These metrics, emphasising the average of the squared differences between predicted and actual values, suggest that the model effectively captures the material's overall temperature trends.

The model demonstrates good predictive performance. However, the relatively high maximum absolute error for maximum temperatures indicates that the model may struggle with accurately predicting extreme values. This could be due to several factors, such as the model not being complex enough to capture the nuances of the maximum temperature behaviour or the training data not sufficiently representing the extremes.

5.2.4. Alumina Silicate

The alumina silicate material (Figure 11, Alumina silicate comparison curves) model is well-adapted to the curve's progress. Even if there are some minimal differences between the actual and predicted minimum temperatures, the curve's deviation is almost null.

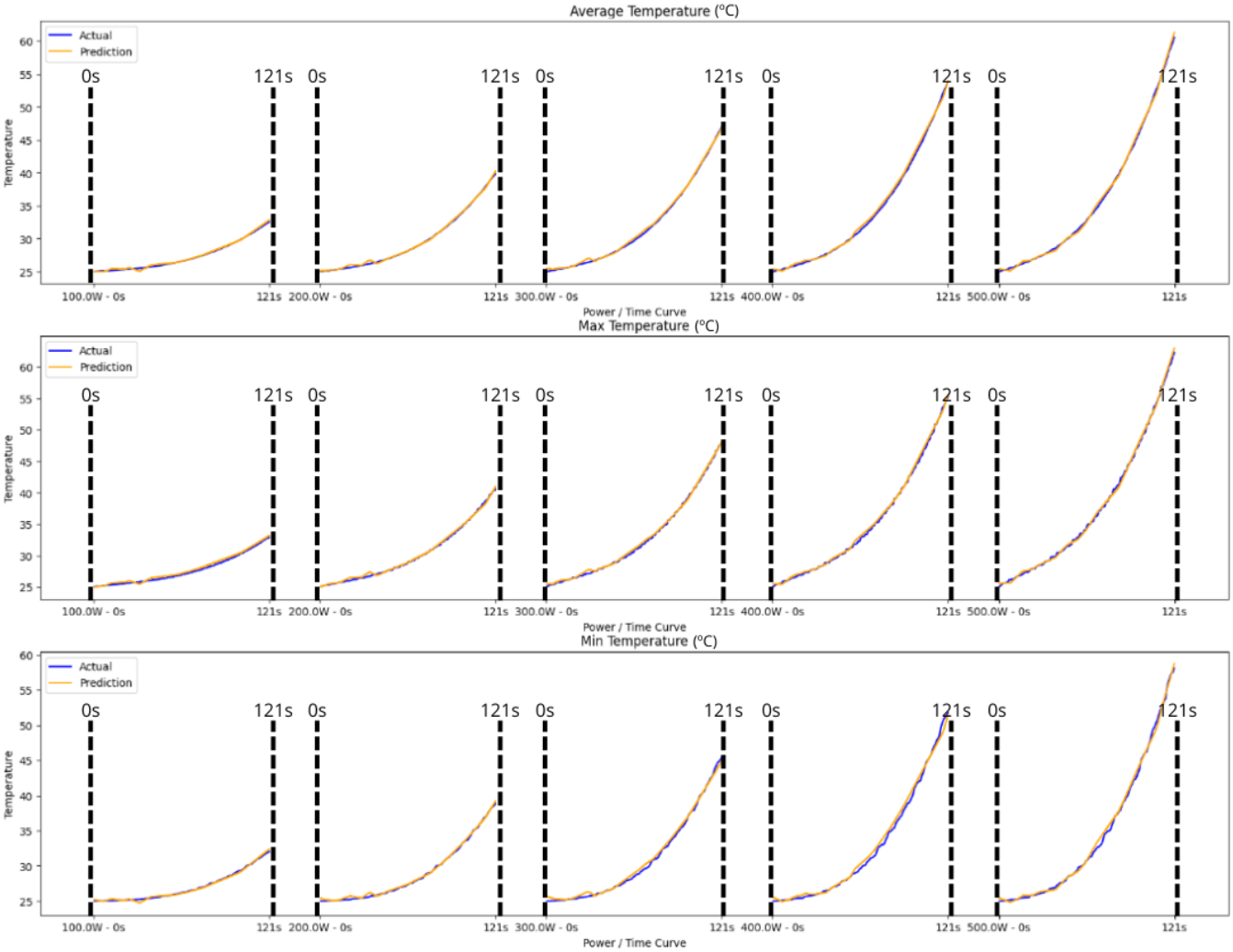

Figure 11. Alumina silicate comparison curves.

Average Temperature Curves

The prediction closely matches the actual temperatures throughout the simulated time, suggesting the model has a solid grasp of the material's heat absorption and dissipation characteristics under varying power inputs.

Maximum Temperature Curves

The predictions here are also closely aligned, slightly under the actual curve at some points. This could indicate the model's conservative nature in estimating peak temperatures but still shows high accuracy.

Minimum Temperature Curves

The prediction is similar to previous ones and strongly follows the actual curve with high fidelity.

The alumina silicate model metrics are provided in Table 7.

Table 7. Alumina silicate model metrics.

	Mean Temperature (°C)	**Max Temperature (°C)**	**Min Temperature (°C)**
Mean Absolute Error	0.501	0.567	0.603
Max Absolute Error	8.243	8.117	9.848
Mean Squared Error	0.736	0.865	0.951

The MAE values of 0.501 °C for mean temperature, 0.567 °C for maximum temperature, and 0.603 °C for minimum temperature indicate the model's high accuracy. Such low MAE figures suggest that, on average, the model's predictions are very close to the actual temperatures, with minimal deviations.

The maximum AE values, standing at 8.243 °C for mean temperature, 8.117 °C for maximum temperature, and 9.848 °C for minimum temperature, show that the model maintains a good degree of accuracy even in the face of the most challenging predictions. These figures highlight the model's robustness and its ability to handle outliers or extreme temperature variations without significant deviations from actual values.

With MSE values of 0.736 °C for mean temperature, 0.865 °C for maximum temperature, and 0.951 °C for minimum temperature, the model demonstrates consistency in its predictive performance. These MSE metrics, emphasising the square of the prediction errors, underscore the model's effectiveness in accurately forecasting temperatures across a spectrum of conditions with a controlled level of error.

These metrics indicate a very well-performing model. The errors are minimal, and even the maximum errors are quite low, which might suggest that the model deals well with outliers or unusual data points.

5.3. Susceptor Materials

5.3.1. SiC

The last group studied were the susceptor materials, starting with SiC, as shown in Figure 12. SiC comparison curves show how well the model adapts to the exponential growth of the material heating curve for each different value. However, the prediction error grows along with the power due to the drastic change in temperature.

Average Temperature Curves

The model's prediction rises sharply and closely follows the actual temperature, indicating a strong initial response. The model captures the rapid increase in temperature, reflecting its understanding of the material's quick thermal reaction to the applied power.

Maximum Temperature Curves

The predictions at higher power settings exhibit a sharp increase that surpasses the actual temperature initially. This could imply that the model expects a faster thermal response from the material than what occurs. Despite this, the model predictions rapidly converge with the actual data, indicating that the correct overall trend is captured.

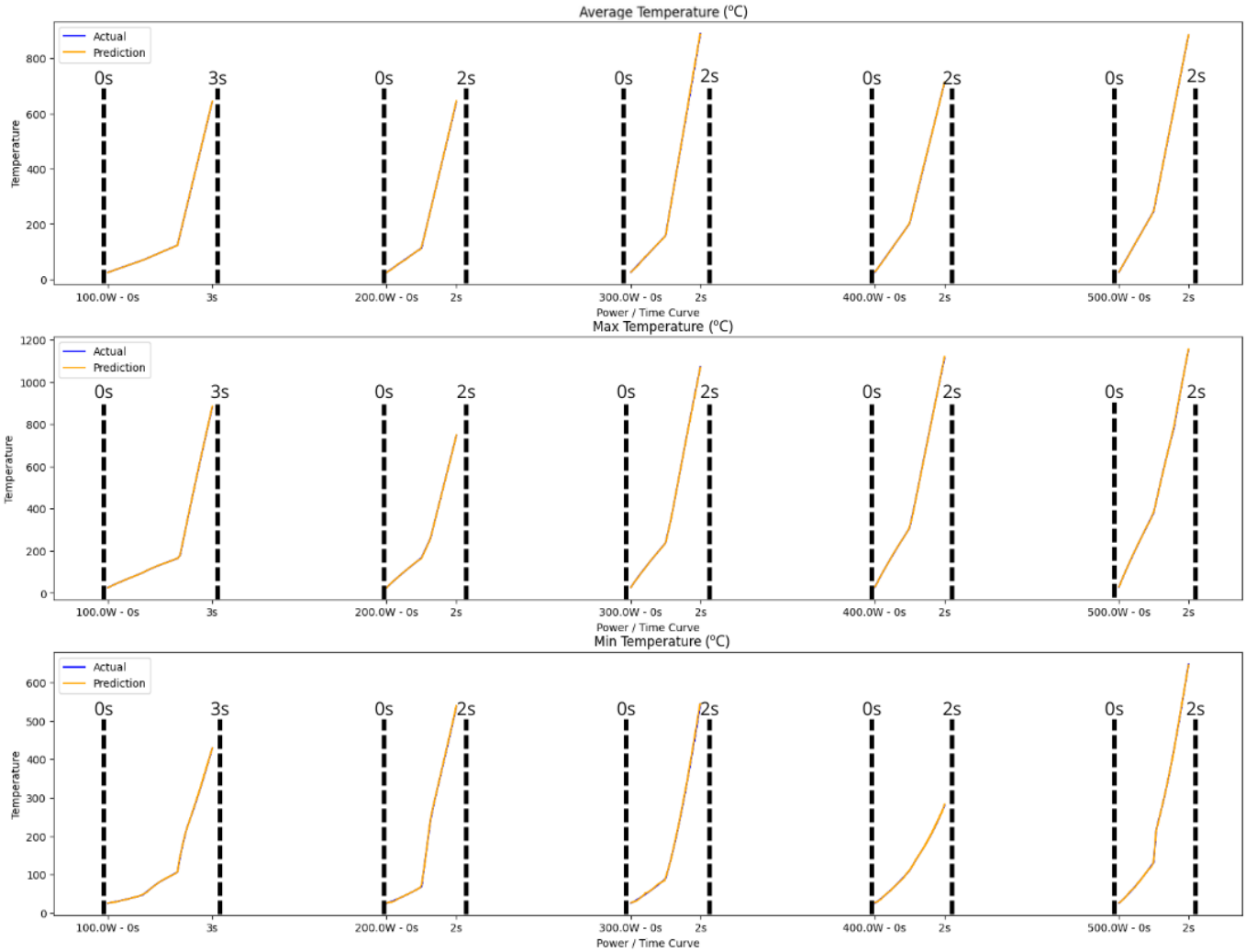

Figure 12. SiC comparison curves.

Minimum Temperature Curves

The prediction starts well-aligned, slightly overestimates, and follows the actual trend. It captures the material's initial temperature behaviour accurately.

Metrics for the SiC model are shown in Table 8.

Table 8. SiC model metrics.

	Mean Temperature (°C)	Max Temperature (°C)	Min Temperature (°C)
Mean Absolute Error	1.190	1.542	1.058
Max Absolute Error	12.134	16.706	10.869
Mean Squared Error	2.781	4.436	2.228

The MAE values of 1.190 °C for mean temperature, 1.542 °C for maximum temperature, and 1.058 °C for minimum temperature demonstrate the model's commendable accuracy in predicting temperature variations. Particularly, the low MAE for minimum temperature suggests the model's strong capability in accurately forecasting lower temperature ranges.

While the maximum AE values (12.134 °C for mean temperature, 16.706 °C for maximum temperature, and 10.869 °C for minimum temperature) highlight the challenges in predicting temperature extremes, they also show the model's ability to maintain reasonable accuracy under diverse conditions.

The MSE values of 2.781 °C for mean temperature, 4.436 °C for maximum temperature, and 2.228 °C for minimum temperature reflect the model's overall consistency and the accuracy of its predictions. These metrics underscore the model's effectiveness in capturing the material's temperature behaviour.

Overall, the model appears to perform well, especially for minimum temperature predictions, with moderate accuracy for mean and maximum temperatures. The higher error metrics for the maximum temperature suggest that the model may not capture extreme values as reliably as it does average or minimum values. This is not uncommon, as extreme values can be more difficult to predict due to their potentially volatile nature.

5.3.2. ALN Compact Powder

The ALN compact powder material behaviour is shown in Figure 13. ALN compact powder comparison curves show that this model is performing reasonably well, particularly for average and minimum temperatures.

Mean Temperature Curves

The predictions are impressively close to the actual temperatures, with the model accurately capturing the sharp rise and overall trend. At higher power settings, the prediction and actual curves tightly align, indicating that the model effectively adapts to the increased energy input.

Maximum Temperature Curves

There is a very close correlation between the predicted and actual temperatures, particularly at the final time, suggesting the model has effectively learned the material's response at these levels of power input.

Minimum Temperature Curves

The model again shows a slight initial lag in the prediction, followed by a tight correspondence with the actual temperature, reflecting the model's capacity to quickly adjust to the material's response.

The metrics for all the curves and model performance are presented in Table 9.

Table 9. ALN compact powder model metrics.

	Mean Temperature (°C)	**Max Temperature (°C)**	**Min Temperature (°C)**
Mean Absolute Error	3.353	6.679	3.797
Max Absolute Error	47.366	114.272	38.01
Mean Squared Error	28.107	119.875	29.520

The MAE values of 3.353 °C for mean temperature, 6.679 °C for maximum temperature, and 3.797 for minimum temperature show that the model is reasonably accurate in its predictions, particularly considering the complex nature of temperature behaviour in this exact material, in which the curves have great variations.

Although the maximum AE values are relatively high, with 47.366 °C for mean temperature, 114.272 °C for maximum temperature, and 38.01 °C for minimum temperature, they offer valuable insights into the model's performance under extreme conditions. These measurements highlight the toughest scenarios where the model's predictions diverge from actual temperatures.

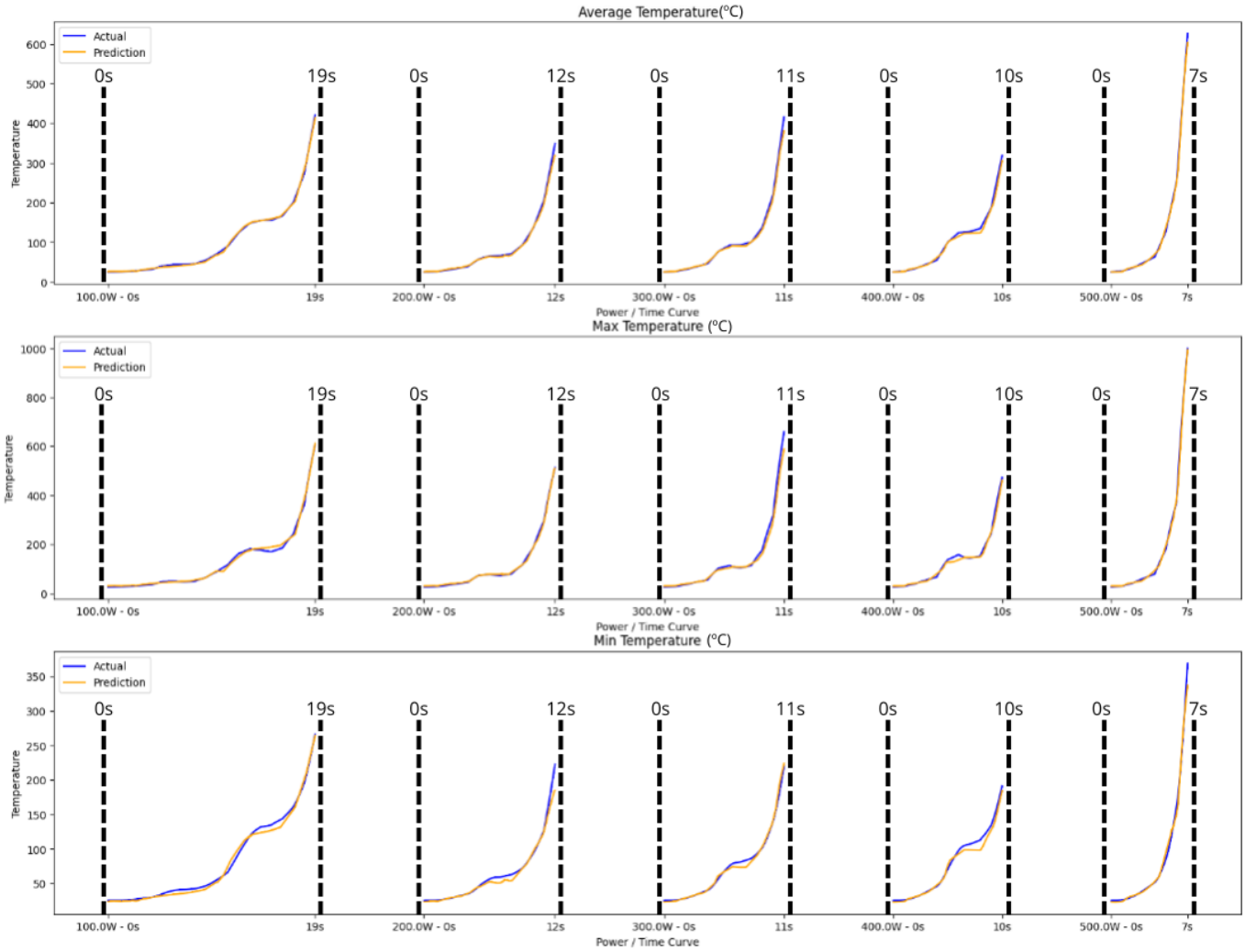

Figure 13. ALN compact powder comparison curves.

The MSE values of 28.107 °C for mean temperature, 119.875 °C for maximum temperature, and 29.520 °C for minimum temperature point out how the abrupt differences in maximum temperatures affect the final result.

As indicated by the lower MAE and MSE values. The maximum temperature predictions are less accurate, which is common in many predictive models, especially if the maximum temperature data have more volatility or less pattern consistency. The higher maximum absolute error values indicate the presence of outlier predictions or instances where the model significantly deviates from the actual values, which might be due to extreme conditions or anomalies in the data that the model has not learned to predict accurately.

5.3.3. CuO

The CuO curves are provided in Figure 14. CuO comparison curves have some particularities. Even if the model can adapt itself to exponential growth when the three curves have different types of growth, the backpropagation of the error from the mean and the maximum temperature curves leads to the minimum temperature curve having some small irregularities at the time of the inference.

Average Temperature Curves

Despite a brief period of overestimation, the model's prediction aligns well with the actual temperature across these power settings. The quick realignment suggests that the model adapts efficiently after recognising its initial prediction error.

Maximum Temperature Curves

This is similar to the mean temperature, with an initial prediction above the actual temperature followed by a closer alignment, showing the model's rapid adjustment capabilities.

Minimum Temperature Curves

The prediction begins well-aligned but then diverges slightly, indicating the model's initial accuracy but suggesting a need for adjustment in response to the material's rate of temperature increase.

CuO model metrics are presented in Table 10.

Table 10. CuO model metrics.

	Mean Temperature (°C)	**Max Temperature (°C)**	**Min Temperature (°C)**
Mean Absolute Error	11.978	15.877	4.486
Max Absolute Error	208.080	349.268	44.788
Mean Squared Error	368.710	876.316	46.591

The MAE values, standing at 11.978 °C for mean temperature, 15.877 °C for maximum temperature, and notably lower at 4.486 °C for minimum temperature, indicate a spectrum of accuracy across different temperature predictions. The model's performance in predicting the minimum temperature with a relatively low error is particularly encouraging, underscoring its capability to accurately capture lower temperature ranges.

While the maximum AE values are considerable (208.080 °C for mean temperature, 349.268 °C for maximum temperature, and 44.788 °C for minimum temperature), they provide a clear benchmark for the model's performance under the most challenging conditions. The significantly lower maximum AE for minimum temperature further accentuates the model's relative strength in this area.

The MSE values (368.710 °C for mean temperature, 876.316 °C for maximum temperature, and 46.591 °C for minimum temperature) reveal areas where the predictive accuracy can be substantially improved. The relatively lower MSE for minimum temperature predictions again highlights this as a strength of the current model, providing a foundation for building upon and extending this accuracy across other temperature ranges.

The metrics suggest that the model is most accurate with the minimum temperature predictions and least accurate with the maximum temperature predictions. The high maximum absolute error in both mean and maximum temperatures could indicate outliers or instances where the model fails to capture extreme values accurately. The differences in these metrics across the three temperature categories may suggest that different aspects of the model's feature extraction or learning process are better suited to capturing certain types of temperature behaviour over others.

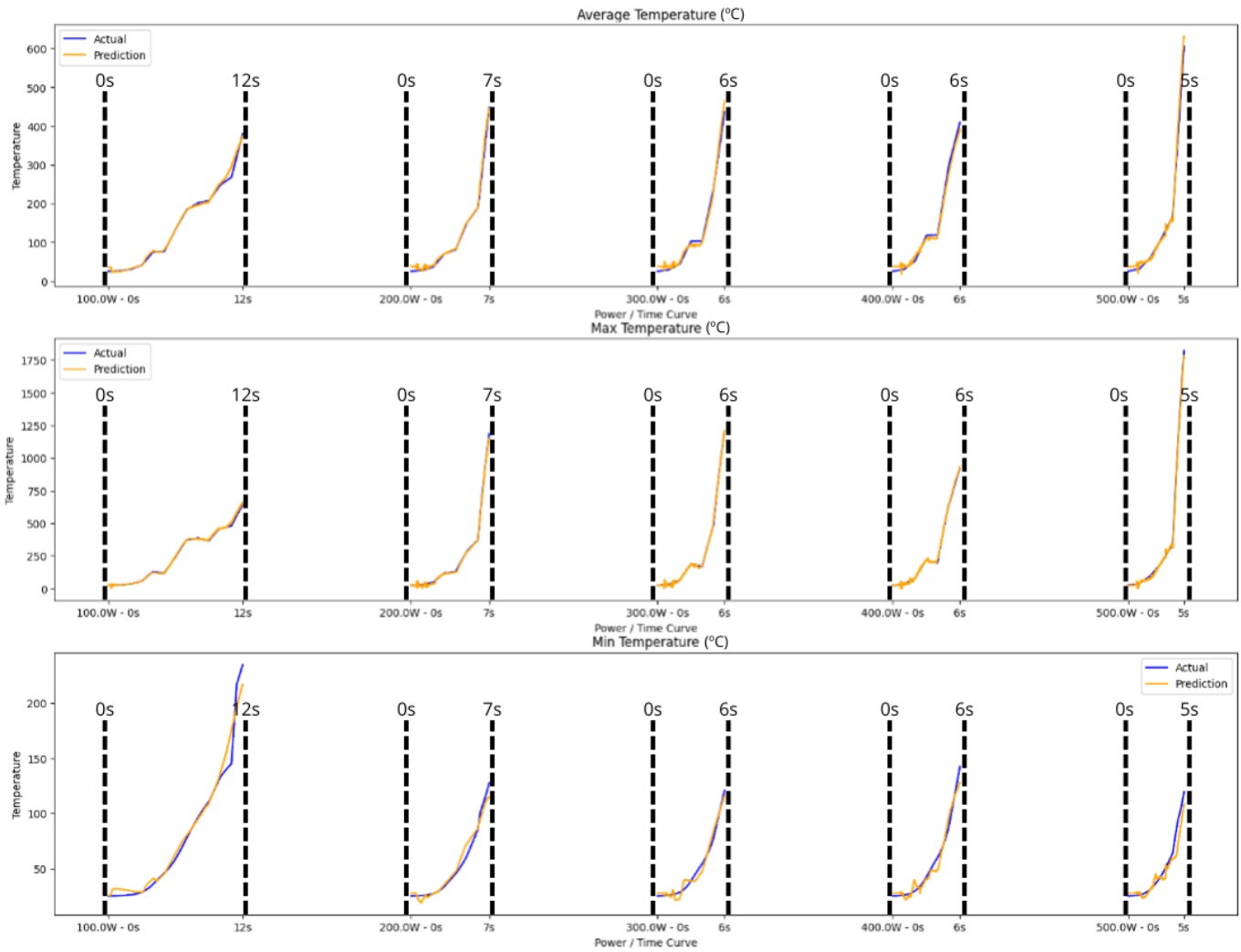

Figure 14. CuO comparison curves.

6. Conclusions

In this study, we have conclusively demonstrated that the adoption of convolutional neural networks (CNNs) in predicting the microwave heating dynamics of materials offers a significant leap forward, achieving a 60-fold acceleration in prediction speed across the nine given materials when compared to traditional simulation techniques. This remarkable enhancement not only underscores the efficiency and scalability of neural networks but also heralds a transformative potential for real-time simulations, reducing computational burdens and facilitating rapid iterations in material design and optimisation processes.

Moreover, our findings highlight a crucial aspect of employing CNNs for the simulation of heating dynamics: the critical need for comprehensive datasets that encompass a wide range of power settings and their corresponding thermal behaviour. The variability in heating curves, which directly correlates with different power levels, underscores the necessity of robust datasets to train the neural networks effectively. This variety in data ensures that the CNNs can accurately predict the temperature curves over time for any given material under various thermal conditions.

It is also imperative to clarify that the predictions made by our CNN models are specifically focused on the temporal evolution of temperature in the materials under study. The ability to predict temperature curves over time with high fidelity is a testament to the sophisticated learning capabilities of convolutional neural networks.

Therefore, while our study has demonstrated the significant advantages of using CNNs to simulate the heating dynamics of materials, it also highlights the indispensable role of comprehensive and diverse datasets. The future of material simulation with CNNs, hence, lies in not only advancing the models and computational techniques but also in the meticulous compilation and utilisation of extensive simulation data covering a wide array of power settings.

Author Contributions: Conceptualization, V.R.N. and L.A.; Data Curation, V.R.N.; Funding Acquisition, L.A.; Investigation, V.R.N.; Methodology, V.R.N.; Project Administration, L.A.; Resources, A.H.; Software, V.R.N. and A.H.; Supervision, L.A., I.R. and I.F.-P.R.; Validation, A.H., I.R. and I.F.-P.R.; Writing—original draft, V.R.N. and L.A.; Writing—review and editing, I.R. and I.F.-P.R. All authors have read and agreed to the published version of the manuscript.

Funding: The GREEN-LOOP project has received funding from the European Union's Horizon Europe (grant number 101057765). Views and opinions expressed are, however, those of the author(s) only and do not necessarily reflect those of the European Union or the European Research Council Executive Agency. Neither the European Union nor the granting authority can be held responsible for them.

Data Availability Statement: The data that support the findings of this study are available from the corresponding author, Luis Acevedo, upon reasonable request.

Conflicts of Interest: All authors are employed by Idener Research and Development A.I.E.

References

1. Hu, Q.; He, Y.; Wang, F.; Wu, J.; Ci, Z.; Chen, L.; Xu, R.; Yang, M.; Lin, J.; Han, L.; et al. Microwave technology: A novel approach to the transformation of natural metabolites. *Chin. Med.* **2021**, *16*, 87. [CrossRef] [PubMed]
2. Acevedo, L.; Ferreira, G.; López-Sabirón, A.M. Exergy transfer principles of microwavable materials under electromagnetic effects. *Mater. Today Commun.* **2021**, *27*, 102313. [CrossRef]
3. Hazervazifeh, A.; Nikbakht, A.M.; Nazari, S. Industrial microwave dryer: An effective design to reduce non-uniform heating. *Eng. Agric. Environ. Food* **2019**, *14*, 110–121. [CrossRef] [PubMed]
4. Metaxas, A.C.; Roger, J.M. *Industrial Microwave Heating*; P. Peregrinus on behalf of the Institution of Electrical Engineers Peter Peregrinus Ltd.: London, UK, 1983.
5. Bhattacharya, M.; Basak, T. Can the container-dielectrics control heating patterns for microwave assisted material processing? A finite element based introspection. *Int. J. Heat Mass Transf.* **2023**, *205*, 123684. [CrossRef]
6. Acevedo, L.; Usón, S.; Uche, J. Numerical study of cullet glass subjected to microwave heating and SiC susceptor effects. Part I: Combined electric and thermal model. *Energy Convers. Manag.* **2015**, *97*, 439–457. [CrossRef]
7. Bhatt, S.C.; Ghetiya, N.D. 3D Multiphysics simulation of microwave heating of bulk metals with parametric variations. *Chem. Eng. Process.-Process Intensif.* **2023**, *184*, 109271. [CrossRef]
8. Yang, R.; Chen, J. Mechanistic and Machine Learning Modeling of Microwave Heating Process in Domestic Ovens: A Review. *Foods* **2021**, *10*, 2029. [CrossRef] [PubMed]
9. Mehdizadeh, M. *Microwave/RF Applicators and Probes for Material Heating, Sensing, and Plasma Generation*; Elsevier: Amsterdam, The Netherlands, 2009.
10. Kazemi, N.; Musilek, P. Comparative Analysis of Machine Learning Techniques for Temperature Compensation in Microwave Sensors. *IEEE Trans. Microw. Theory Tech.* **2021**, *69*, 4223–4236. [CrossRef]
11. Yang, Y.; Shahbeik, H.; Shafizadeh, A.; Masoudnia, N.; Rafiee, S.; Zhang, Y.; Pan, J.; Tabatabaei, M.; Aghbashlo, M. Biomass microwave pyrolysis characterization by machine learning for sustainable rural biorefineries. *Renew. Energy* **2022**, *201*, 70–86. [CrossRef]
12. Okafor, C.E.; Okafor, E.J.; Ikebudu, K.O. Evaluation of machine learning methods in predicting optimum tensile strength of microwave post-cured composite tailored for weight-sensitive applications. *Eng. Sci. Technol. Int. J.* **2022**, *25*, 100985. [CrossRef]
13. Yang, R.; Wang, Z.; Chen, J. An Integrated Approach of Mechanistic-Modeling and Machine-Learning for Thickness Optimization of Frozen Microwaveable Foods. *Foods* **2021**, *10*, 763. [CrossRef] [PubMed]
14. Stankovic, Z.; Milovanovic, B.; Doncov, N.; Milijic, M. Microwave applicators modeling—Alternative approaches based on neural networks incorporating domain knowledge. In Proceedings of the 10th Symposium on Neural Network Applications in Electrical Engineering, Belgrade, Serbia, 23–25 September 2010; pp. 81–88.
15. Kireeva, N.; Solov'Ev, V.P. Machine learning analysis of microwave dielectric properties for seven structure types: The role of the processing and composition. *J. Phys. Chem. Solids* **2021**, *156*, 110178. [CrossRef]
16. Taflove, A.; Hagness, S.C.; Piket-May, M. 9—Computational Electromagnetics: The Finite-Difference Time-Domain Method. In *The Electrical Engineering Handbook*, 3rd ed.; Chen, E., Ed.; Academic Press: Burlington, NJ, USA, 2005; pp. 629–670.

17. Taheri, S.; McFarlane, D.J.; Mattner, S.W.; Brodie, G.I. Potential of Microwave Heating and Plasma for Biosecurity Applications. *Thermo* **2022**, *2*, 312–333. [CrossRef]
18. Roger, J.M. *Engineers' Handbook of Industrial Microwave Heating*; Institution of Engineering and Technology (IET): Stevenage, UK, 1998.
19. Zhang, P.; Hu, Y.; Jin, Y.; Deng, S.; Wu, X.; Chen, J. A Maxwell's Equations Based Deep Learning Method for Time Domain Electromagnetic Simulations. *IEEE J. Multiscale Multiphys. Comput. Tech.* **2021**, *6*, 35–40. [CrossRef]
20. Budd, C.; Hill, A.; Hooper, G. Modelling microwave cooking; theory and experiment. *Appl. Math. Model* **1996**, *20*, 3–16.
21. Taflove, A. *Computational Electrodynamics: The Finite-Difference Time-Domain Method*, Artech House: Boston, MA, USA, 1995; ISBN 1-58053-832-0. Available online: https://github.com/cvarin/FDTD/blob/master/Taflove/fdtd1D.m (accessed on 29 July 2024).
22. Acevedo, L.; Usón, S.; Uche, J. Local exergy cost analysis of microwave heating systems. *Energy* **2015**, *80*, 437–451. [CrossRef]
23. Velastegui, R.; Zhinin-Vera, L.; Pilliza, G.E.; Chang, O. Time Series Prediction by Using Convolutional Neural Networks. In Proceedings of the Future Technologies Conference (FTC), Vancouver, BC, Canada, 5–6 November 2020; Springer: Cham, Germany, 2021; Volume 1, pp. 499–511. [CrossRef]
24. Ayeni, J.A. Convolutional Neural Network (CNN): The architecture and applications. *Appl. J. Phys. Sci.* **2022**, *4*, 42–50. [CrossRef]
25. Thakur, A. Keras Dense Layer: How to Use It Correctly. Available online: https://wandb.ai/ayush-thakur/keras-dense/reports/Keras-Dense-Layer-How-to-Use-It-Correctly--Vmlldzo0MjAzNDY1#:~:text=A%20dense%20layer%20is%20mostly,to%20a%20new%20dimension%20d1 (accessed on 9 March 2024).
26. la Tour, T.D.; Eickenberg, M.; Nunez-Elizalde, A.O.; Gallant, J.L. Feature-space selection with banded ridge regression. *NeuroImage* **2022**, *264*, 119728. [CrossRef]
27. Berrar, D. Cross-Validation. *Encycl. Bioinform. Comput. Biol.* **2019**, *1*, 542–545. [CrossRef]

Disclaimer/Publisher's Note: The statements, opinions and data contained in all publications are solely those of the individual author(s) and contributor(s) and not of MDPI and/or the editor(s). MDPI and/or the editor(s) disclaim responsibility for any injury to people or property resulting from any ideas, methods, instructions or products referred to in the content.